Automatically tying well logs to seismic data

Andrew Muñoz & Dave Hale
Center for Wave Phenomena, Colorado School of Mines, Golden, CO 80401, USA

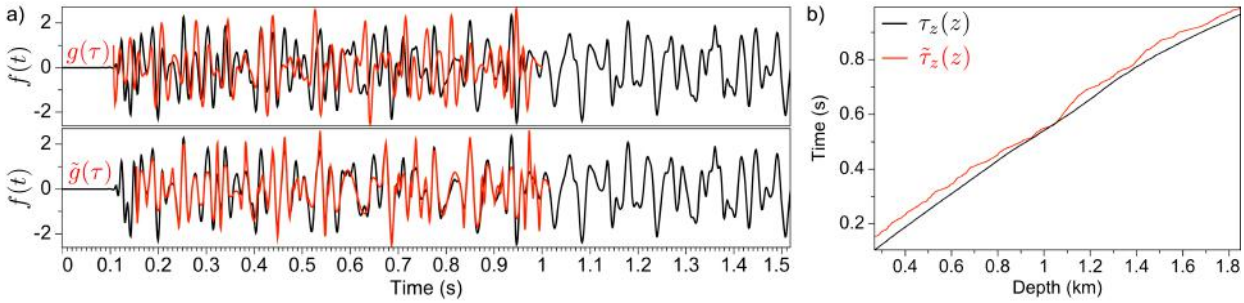

Figure 1. Original and tied synthetic seismogram overlaid on a seismic trace. $f(t)$ is a seismic trace (black) extracted from the time-migrated Teapot Dome 3D seismic image. $g(\tau)$ is a synthetic seismogram (red) generated from Teapot Dome well logs. $\tilde{g}(\tau)$ is the same synthetic seismogram (red) automatically tied to the seismic trace using dynamic time warping. We compare the initial and updated time-depth functions in (b). The initial time-depth function $\tau_z(z)$ (black) is computed from equation 2 using a well log; the updated time-depth function $\tilde{\tau}_z(z)$ (red) is computed using dynamic time warping.

ABSTRACT
Seismic data are recorded and commonly interpreted in vertical two-way time; well logs, measured in depth, must be tied to seismic using a time-depth curve. However, well ties contain a large amount of uncertainty due to errors in the generation of synthetic seismograms and manual matching of synthetic seismograms to seismic traces. Using dynamic time warping, a fast algorithm that optimally aligns two sequences, we shift and warp a synthetic seismogram to match a seismic trace to produce a well tie and time-depth function.

Key words: seismic well logs tie time depth conversion

1 INTRODUCTION

Making well ties has long been considered an art for geophysical interpreters (White and Simm, 2003). The process involves seismic image processing, wavelet creation, estimation of the time-depth curve, geologic interpretation, and manual corrections. Each step in generating a well tie may require quantitative analysis, but ultimately creating a well tie is a lengthy and interpretive process with potential for significant human error.

We use an algorithm commonly used in speech recognition called dynamic time warping (DTW) (Mueller, 2007) to *quantitatively* and *quickly* compute well ties and time-depth functions. Figure 1a shows a synthetic seismogram before and after DTW; visually, the tied synthetic matches the seismic trace. This alignment yields an updated time-depth function shown in Figure 1b.

Integrating well logs and seismic data is crucial when estimating subsurface properties. Many procedures for tying well logs to seismic data exist (e.g., Walden and White (1984); White and Hu (1997); White and Simm (2003); Duchesne and Gaillot (2011); Edgar and van der Baan (2011)). Also, many commercial software packages enable seismic interpreters to generate well ties from well logs and seismic traces. They provide graphical interfaces that allow the user to interactively shift, stretch, and squeeze synthetic seismograms to match time-migrated seismic traces. While the user manually matches synthetics to seismic traces, the software automatically updates a time-depth curve. How-

ever, this process is tedious and relies on the skill and experience of the user.

Steps common to most well tie processing include:

(i) compute reflectivity from sonic and density logs
(ii) convert reflectivity from depth to time
(iii) convolve an estimated wavelet with reflectivity
(iv) match the synthetic with the seismic trace
(v) update the time-depth curve

This paper describes a similar sequence of steps, but we use DTW to correct errors associated with rough estimates of the wavelet and time-depth conversion.

2 SYNTHETIC SEISMOGRAM

The freely available Teapot Dome 3D time-migrated seismic image (Anderson, 2009) has been rotated, trimmed, and resampled spatially, as described by Hale (2010). This data set contains hundreds of well logs that are also described in Hale (2010). Here we use logs from only one well.

2.1 Well logs

A well with a velocity log and density log is required to generate a synthetic seismogram. We use well UWI 490252305400, which has a P-wave velocity log and a density log. The logs span depths from 0.28 km to 1.85 km. Figure 2 shows the velocity, density, and computed reflectivity logs. The velocity log $v(z)$ and the density log $\rho(z)$ are uniformly sampled functions of depth for $z = z_0, z_0 + \Delta z, \ldots, z_0 + (N_z - 1)\Delta z$. Let

$$r(z) = \frac{v(z+\Delta z)\rho(z+\Delta z) - v(z)\rho(z)}{v(z+\Delta z)\rho(z+\Delta z) + v(z)\rho(z)} \qquad (1)$$

denote the acoustic reflection coefficient for normal-incidence P-waves.

This reflectivity is an approximation based on the acoustic impedance and assumes normal incidence. If there is a significant amplitude variation with offset in the seismic data, using elastic impedance to generate reflectivity would be more accurate (Connolly, 1999).

The reflectivity is sampled with a log interval of $\Delta z = 6$ inches, while the seismic trace is sampled with $\Delta t = 4$ ms (roughly every 4 m, depending on seismic velocities). We combine a wavelet with the reflectivity to generate a synthetic seismogram.

2.2 Wavelet estimation

The seismic wavelet is complicated in that it varies with time, space, and frequency. This makes the generation of an accurate wavelet a difficult task (Angeleri, 1983). The wavelet has a significant effect on the synthetic seismogram; even if the logs used to compute reflectivity were accurately calibrated and corrected for errors, an inaccurate wavelet would thwart many well tie processes (Edgar and van der Baan, 2011). Many wavelet approximation methods exist (e.g., Angeleri (1983); Walden and White (1984); Duchesne and Gaillot (2011); Edgar and van der Baan (2011)), however, each method is prone to human error.

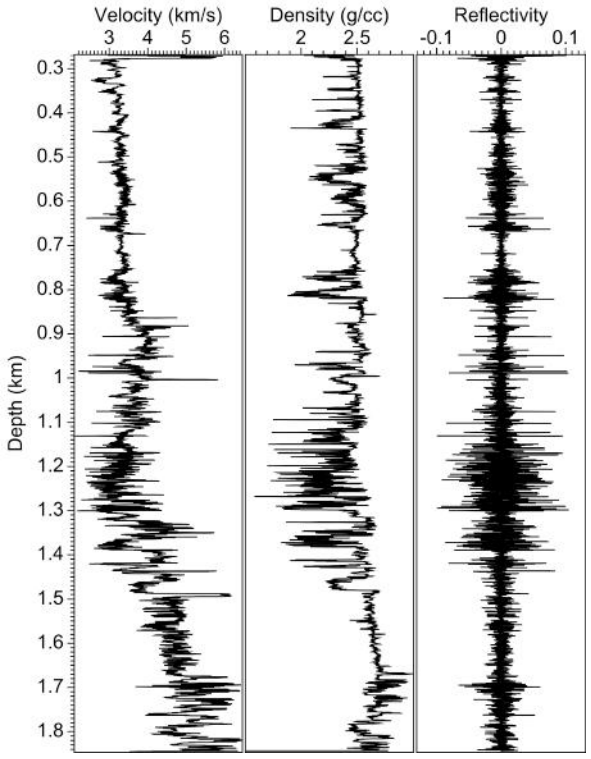

Figure 2. Teapot Dome well UWI 490252305400 has a P-wave velocity log and density log. Acoustic reflectivity in the rightmost panel is computed using equation 1.

Two common methods for wavelet extraction are statistical and deterministic well-tie methods (Edgar and van der Baan, 2011). The deterministic well-tie methods require that a well-tie already exists, while the statistical method extracts an average wavelet from a specified window of 3D seismic data (Edgar and van der Baan, 2011).

A simpler approach is to assume a constant wavelet with a peak frequency equal to that of the seismic trace. Figure 3a illustrates a Ricker wavelet with a peak frequency of 35 Hz. This peak frequency is computed from the amplitude spectrum of the seismic trace nearest to the well.

Before we combine a wavelet with the reflectivity, we compute an initial time-depth relationship. Initial time-depth curves are estimated most commonly using the P-wave velocity log and check shots, if available (Edgar and van der Baan, 2011). We follow the common practice of using the P-wave velocity log $v(z)$ to

compute vertical-two way reflection time:

$$\tau_z(z) = \tau_0 + 2\int_{z_0}^{z} \frac{d\xi}{v(\xi)}, \tag{2}$$

where τ_0 is the best estimate of vertical two-way time to depth z_0, the shallowest depth sampled for the velocity log. The subscript z reminds us that the two-way time $\tau_z(z)$ is a sampled function of depth z.

Using $\tau_z(z)$ (and ignoring attenuation, multiple reflections, and other effects), we compute a synthetic seismogram $g_0(\tau)$ as a simple superposition of seismic wavelets $w(\tau)$, each delayed by a reflection time $\tau_z(z)$ and weighted by a corresponding reflectivity $r(z)$ from equation 1:

$$g_0(\tau) = \int_{z_0}^{z} r(\xi)\, w[\tau - \tau_z(\xi)]\, d\xi, \tag{3}$$

which we sample uniformly at times $\tau = \tau_0, \tau_0 + \Delta t, \ldots, \tau_0 + (N_\tau - 1)\Delta t$. We use $g_0(\tau)$ to denote the synthetic before amplitude normalization, which is discussed in the next section. Figure 3 shows the wavelet, reflectivity, and synthetic seismogram.

2.3 Amplitude normalization

Attenuation in seismic data can cause significant amplitude changes with depth. We therefore use normalization to scale amplitudes in the synthetic seismogram to be similar to amplitudes in the seismic trace. This normalization is time varying. We simply divide each sample by the rms of values nearby.

The amplitude normalization is applied to the seismic trace $f_0(t)$ and the synthetic seismogram $g_0(\tau)$, as shown in Figure 4. The normalization has a negligible effect on the seismic trace indicating that the seismic trace is already normalized and any noticeable attenuation was previously removed. However, normalization of the synthetic seismogram has a greater effect on its amplitudes, primarily because the amplitude of the wavelet used to generate the seismogram is incorrect. After normalization, amplitudes in the synthetic $g(\tau)$ and seismic trace $f(t)$ are comparable.

3 DYNAMIC TIME WARPING

We find a well tie and updated time-depth function using dynamic time warping. Dynamic time warping (DTW) is an algorithm that finds the optimal warping path between two sequences (Mueller, 2007). DTW utilizes dynamic programming to break up an optimization problem into many smaller subproblems, thereby significantly reducing the computational complexity. Thorough explanations of the algorithm are provided in Hale (2012) and Mueller (2007). We follow the three-step process outlined by Mueller (2007).

To align a synthetic seismogram $g(\tau)$ with a seismic

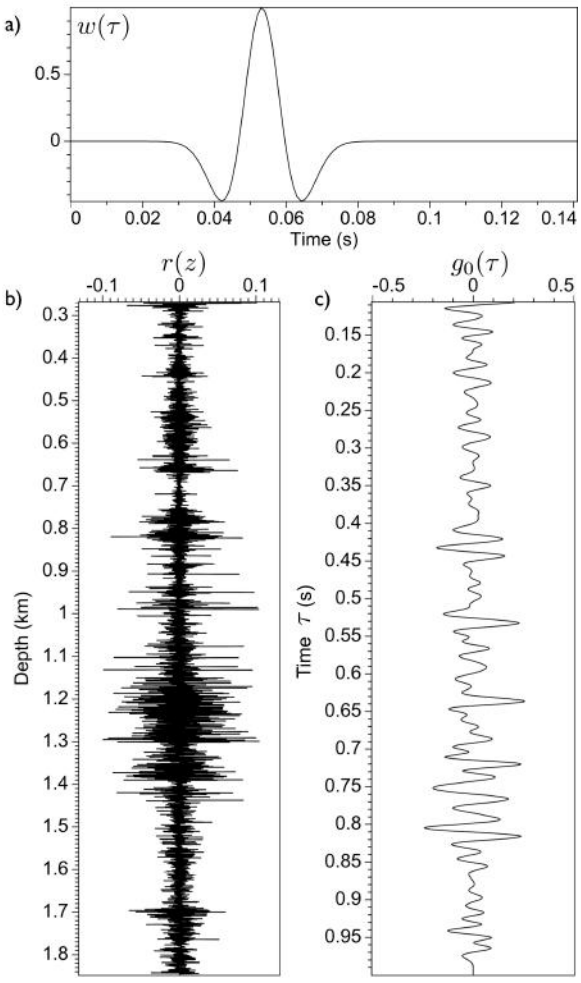

Figure 3. The wavelet $w(\tau)$ (a) is a constant Ricker wavelet with a peak frequency of 35 Hz. The reflectivity $r(z)$ (b) is computed using equation 1. The synthetic seismogram $g_0(\tau)$ (c) is computed using equation 3.

trace $f(t)$, we use DTW to compute a mapping between τ and t such that

$$f(t) \approx g(\tau). \tag{4}$$

We use the two artificially generated sequences shown in Figure 5 to demonstrate DTW.

The first step in DTW is to compute an array of squared alignment errors:

$$e_{i,j} = e(t_i, \tau_j) = [f(t_i) - g(\tau_j)]^2, \tag{5}$$

for all sampled times $t_i = t_0 + i\Delta t, i = 0, 1, \ldots, N_t - 1$, and $\tau_j = \tau_0 + j\Delta t, j = 0, 1, \ldots, N_\tau - 1$. The array of errors $e_{i,j}$, computed for the sequences in Figure 5, is shown in Figure 6a.

The second step is to recursively accumulate the errors to obtain an array of distances (Hale, 2012). We

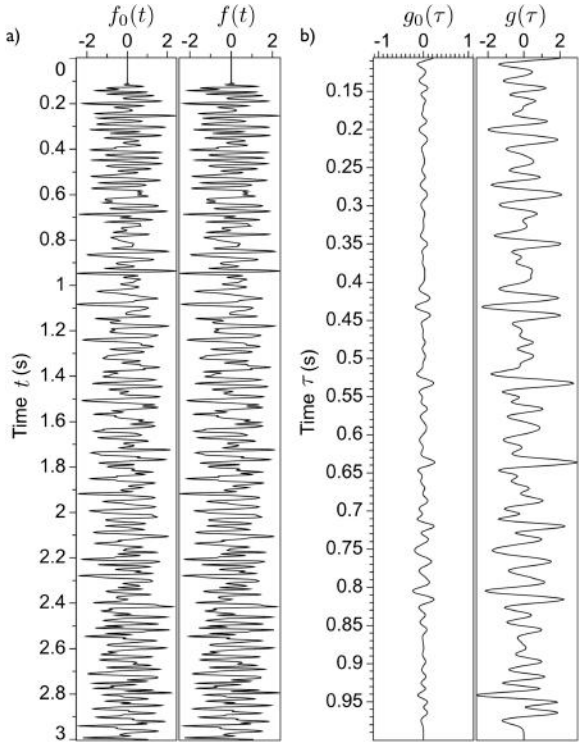

Figure 4. The difference between the seismic trace before and after ($f_0(t)$ and $f(t)$) normalization (a) is negligible. The difference between the synthetic seismogram before and after ($g_0(\tau)$ and $g(\tau)$) normalization (b) is significant.

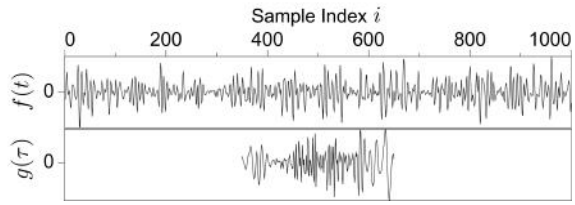

Figure 5. Artificial sequences used to illustrate DTW, where the sequence $g(\tau)$ is a warped and bulk shifted segment of the sequence $f(t)$.

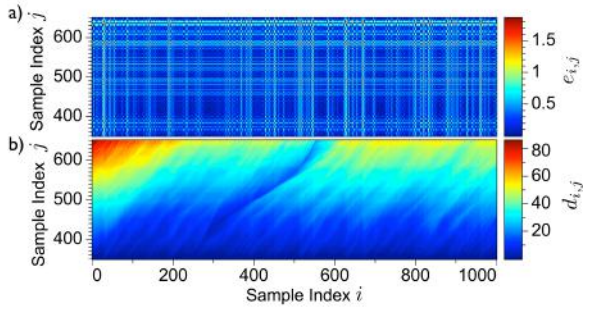

Figure 6. The array of squared alignment errors (a) for the two sequences in Figure 5. The array of distances (b) is defined by equations 6 and 7. A path with small alignment errors is apparent between sample indices of $i = 250$ and $i = 550$.

first initialize:

$$
\begin{aligned}
d_{0,0} &= e_{0,0} \\
d_{0,j} &= e_{0,j} + d_{0,j-1};\ j = 1, 2, \ldots, N_\tau - 1 \\
d_{i,0} &= e_{i,0};\ i = 1, 2, \ldots, N_t - 1 \\
d_{1,j} &= e_{1,j} + \min \begin{cases} d_{0,j} \\ d_{0,j-1} \\ d_{1,j-1} \end{cases} ;\ j = 1, 2, \ldots, N_\tau - 1 \\
d_{i,1} &= e_{i,1} + \min \begin{cases} d_{i,0} \\ d_{i-1,0} \\ d_{i-1,1} \end{cases} ;\ i = 1, 2, \ldots, N_t - 1, \quad (6)
\end{aligned}
$$

which represent distances for samples near the edges of the array (Mueller, 2007). Then, for all $i > 1$ and $j > 1$, we compute:

$$
d_{i,j} = e_{i,j} + \min \begin{cases} d_{i-1,j-1} \\ d_{i-1,j-2} + e_{i,j-1} \\ d_{i-2,j-1} + e_{i-1,j} \end{cases} . \qquad (7)
$$

The resulting array of distances $d_{i,j}$ is shown in Figure 6b.

The third step is to backtrack in the array of distances $d_{i,j}$. We denote the top row of the array of distances by total distances $D_i = d_{i,N_\tau - 1}$, and we set indices $i^\star = \arg\min_i D_i$ and $j^\star = N_\tau - 1$ from which we backtrack to obtain a sequence of sample-index pairs $(i^\star, j^\star)$ (a warping path) that minimizes the distances. From the initial $(i^\star, j^\star)$, we find the smallest of three values from the right side of equation 7 and extend the warping path with the corresponding sample-index pairs. If the smallest value is $d_{i^\star-1,j^\star-1}$, the next sample-index pair is $(i^\star - 1, j^\star - 1)$. If the smallest value is $d_{i^\star-1,j^\star-2} + e_{i^\star,j^\star-1}$, the next sample-index pairs are $(i^\star, j^\star - 1)$ and $(i^\star - 1, j^\star - 2)$. If the smallest value is $d_{i^\star-2,j^\star-1} + e_{i^\star-1,j^\star}$, the next sample-index pairs are $(i^\star - 1, j^\star)$ and $(i^\star - 2, j^\star - 1)$. Notice that we add two new sample-index pairs to the sequence for two of the choices. We then recursively compute the next pair of indices from either $(i^\star - 1, j^\star - 1)$, $(i^\star - 1, j^\star - 2)$, or

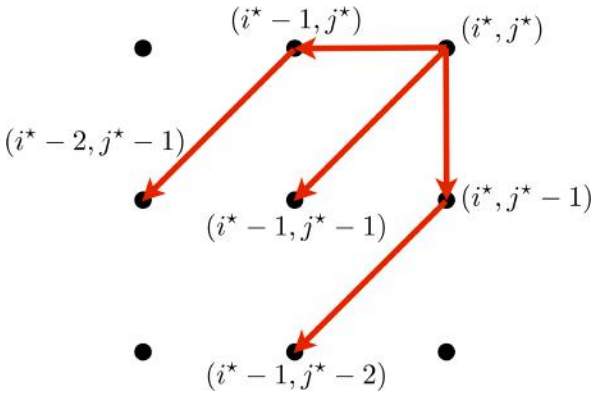

Figure 7. A schematic of the potential warping paths from $(i^\star, j^\star)$ in the backtracking procedure. Black dots represent samples in the array of distances, while red arrows are potential additions to the warping path.

$(i^\star-2, j^\star-1)$ (depending on the smallest corresponding value previously found) until either $i^\star = 0$ or $j^\star = 0$. Figure 7 illustrates the sample-index pairs and potential warping paths in the backtracking procedure. The distance computation and backtracking procedures include constraints described by Sakoe and Chiba (1978). These do not allow warping paths to have long horizontal or vertical segments.

Note that the values of D_i are sums of squared alignment errors, but that some total distances D_i are computed from fewer errors than others, potentially making them smaller. Hence, we must normalize by the number of samples that contribute to each D_i by first backtracking from all samples $(i, N_\tau - 1)$ for $i = 1, 2, \ldots, N_t - 1$, and dividing each D_i by its backtracked path length. This normalization removes the bias of path length and results in a new array of normalized total distances $\hat{D}_i$. We then compute new indices $i_n^\star = \arg\min_i \hat{D}_i$ and $j_n^\star = N_\tau - 1$ from which we backtrack to obtain an optimal warping path.

Figure 8a shows the array of distances with paths backtracked from every sample in D_i. We divide each sample in D_i by its corresponding path length to obtain $\hat{D}_i$ shown in Figure 8b. We then backtrack again from the smallest value of $\hat{D}_i$ to obtain the optimal warping path in Figure 8c.

For the artificial example, the backtracked path from the sample corresponding to the smallest value of $\hat{D}_i$ is consistent with the optimal warping path shown in Figure 8c. The warping path resembles the sinusoidal warping used to generate $g(\tau)$, and the algorithm correctly computes $\tau_0^\star$, the updated τ_0. This solution is confirmed by Figure 9, where the warped $\tilde{g}(\tau)$ is overlaid on the original sequence $f(t)$, and the two sequences match precisely.

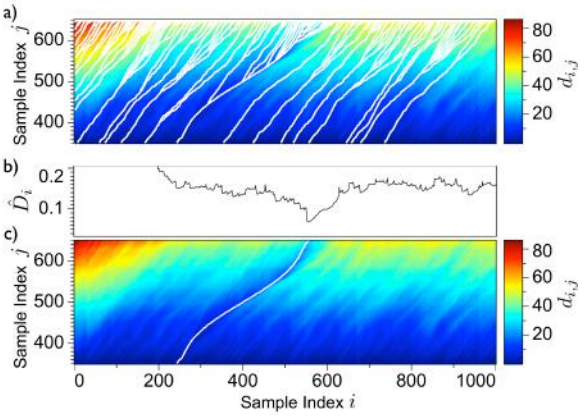

Figure 8. Paths backtracked (a) from every sample in the top row overlaid on the array of distances. Values in the normalized top row of the array of distances $\hat{D}_i$ (b) have a clear minimum. The optimal warping path (c) corresponds to the smallest value of $\hat{D}_i$ and follows valleys of distances.

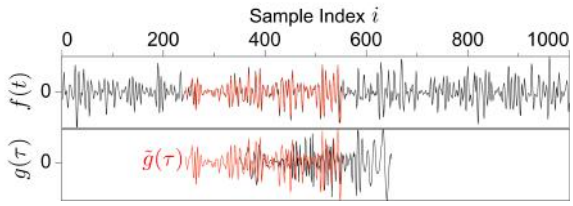

Figure 9. The artificial sequences as shown in Figure 5. $g(\tau)$ is a warped and shifted segment of $f(t)$. Using the DTW optimal warping path (Figure 8c), $g(\tau)$ is corrected to $\tilde{g}(\tau)$.

4 TEAPOT DOME DATA

We next apply the DTW algorithm to a Teapot Dome synthetic seismogram $g(\tau)$ and seismic trace $f(t)$. We find the arrays of errors and distances shown in Figure 10. The optimal path is not easily seen as it was for the artificial example in Figure 6b. The lack of an obvious optimal path is attributed to the shortcomings in the simple process used to compute the synthetic seismogram $g(\tau)$.

We use the same backtracking and path length normalization procedure to compute $\hat{D}_i$ in Figure 10b. We also apply additional constraints to the warping paths as seen in Figure 11c. We assume the entire synthetic seismogram can be tied to the seismic trace, so the optimal warping path must span $j = 0$ to $j = N_\tau - 1$. Also, the synthetic seismogram must be within a window of the seismic trace corresponding to reasonable velocities for the log's depth. We limit the range of velocities from 1.5 km/s to 7 km/s; the velocity log in Figure 2 validates this range as reasonable. These constraints limit the number of potential warping paths. Notice the large reduction in the number of warping paths from Figure 11a to Figure 11c.

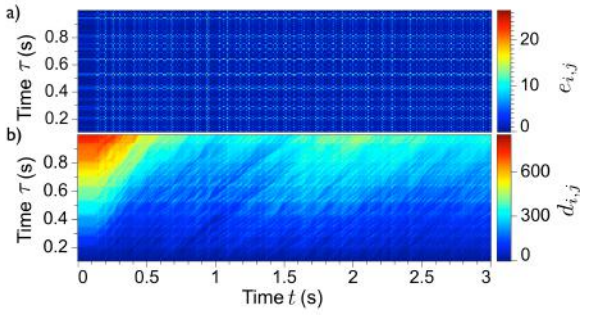

Figure 10. The array of squared alignment errors (a) and distances (b) for the Teapot Dome data. Times t correspond to the seismic trace, and times τ correspond to the synthetic.

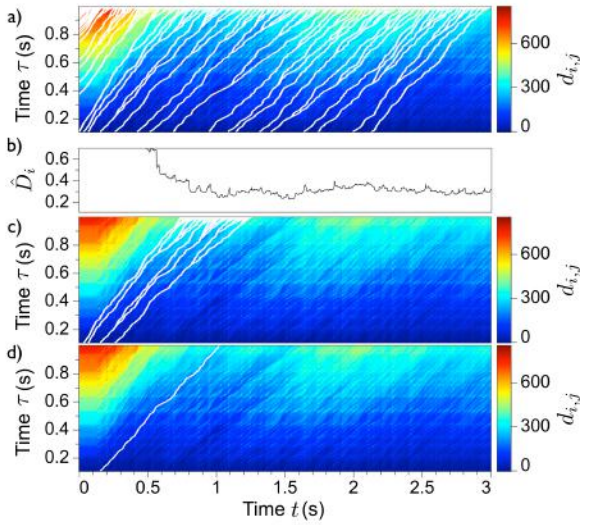

Figure 11. Paths backtracked (a) from every sample in the top row overlaid on the array of distances. Values in the normalized top row of the array of distances $\hat{D}_i$ (b) do not display a clear minimum. Additional time constraints reduce (c) the number of potential warping paths. The optimal warping path (d) corresponds to the smallest value of $\hat{D}_i$ and follows valleys of distances. All of these results are for an 84-degree phase rotation of the synthetic seismogram.

We apply a constant phase rotation to the synthetic seismogram to roughly approximate the seismic trace phase. The optimal path shown in Figure 11d corresponds to the minimum $\hat{D}_i$ for an 84-degree phase rotation (as described in the next section) in the synthetic seismogram.

4.1 Well tie

From the optimal sequence of sample-index pairs $(i^\star, j^\star)$ (warping path), we compute two uniformly sampled and monotonically increasing functions $\tau^\star(t)$ and $t^\star(\tau)$ from each pair of indices where $f(t_{i^\star}) \approx g(\tau_{j^\star})$.

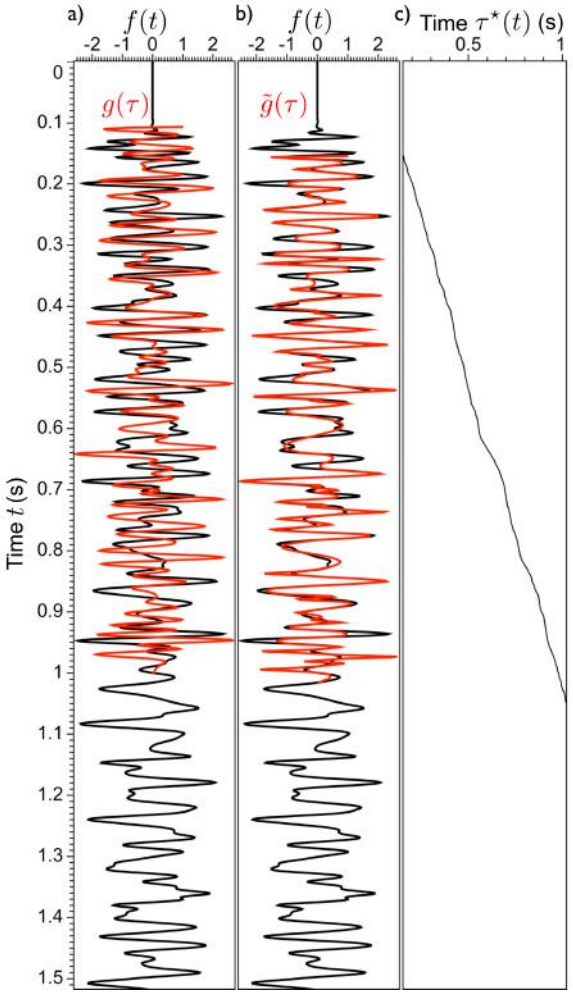

Figure 12. The original synthetic $g(\tau)$ (a) is overlaid on a portion of the seismic trace $f(t)$. The warped synthetic $\tilde{g}(\tau)$ (b) has an 84 degree phase rotation. $\tau^\star(t)$ (c) is the function used to warp the synthetic seismogram.

To optimally match the synthetic seismogram $g(\tau)$ to the seismic trace $f(t)$, we use $\tau^\star(t)$ (Figure 12c):

$$\tilde{g}(t) = g(\tau = \tau^\star(t)) \tag{8}$$

for a range of times $t \in [t_{\min}, t_{\max}]$ defined by the backtracking step in DTW; $t_{\max}$ and $t_{\min}$ correspond to the first and last sample-index pairs of the backtracked path respectively. In Figure 12b, we show the warped synthetic $\tilde{g}(\tau)$ overlaid on the seismic trace $f(t)$ to illustrate the alignment. Figure 12a shows the original synthetic $g(\tau)$ overlaid on the seismic trace $f(t)$ to illustrate the alignment before warping. The warped synthetic is better aligned than the original synthetic.

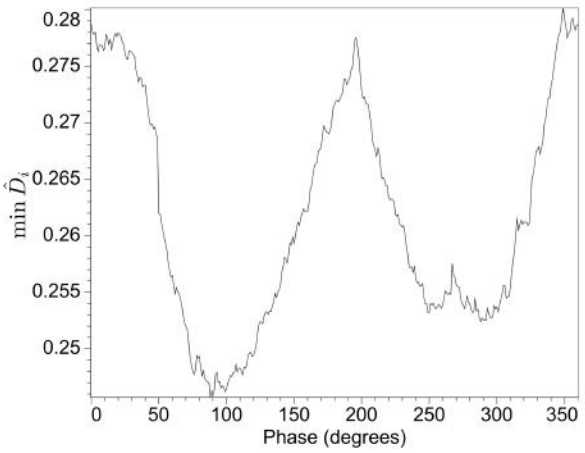

Figure 13. The minimum value of $\hat{D}_i$ (a) varies with a constant phase rotation applied to the synthetic seismogram. We choose the phase to be 84 degrees, because that constant phase rotation yields the smallest value of min $\hat{D}_i$.

4.2 Phase rotation

The phase of the synthetic seismogram should match the phase of the seismic data, but we do not know the seismic wavelet. We approximated the amplitude spectrum by choosing the peak frequency of a Ricker wavelet to match that of the seismic trace. We now approximate the phase with a constant phase rotation that is frequency-independent.

We use DTW to see the effect that phase has on the minimum value of $\hat{D}_i$ with the goal of further reducing $\hat{D}_i$. We rotate the phase of the synthetic by 1 degree and measure the minimum $\hat{D}_i$ within the constraints illustrated by Figure 11c. For a 1-degree constant phase rotation, we do not expect the warping path to change drastically, so we apply the constant phase rotation in 1-degree increments for 360 degrees as shown in Figure 13; for each 1-degree increment, we measure the minimum $\hat{D}_i$. At an 84-degree phase rotation $\hat{D}_i$ is minimized.

4.3 Time-depth function

As stated previously, from the optimal warping path we obtain $t^\star(\tau)$, and can easily compute a new time-depth function:

$$\tilde{\tau}_z(z) = t^\star(\tau = \tau_z(z)), \tag{9}$$

where $\tau_z(z)$ is the initial time-depth function computed from equation 2. If $t^\star(\tau) = \tau$, implying that no warping was necessary, then we obtain $\tilde{\tau}_z(z) = \tau_z(z)$, as expected.

Figure 1b compares $\tilde{\tau}_z(z)$ and $\tau_z(z)$. There is a significant difference between the shape of the two curves and between τ_0 and $\tau_0^\star$. Future work will further explore the differences of the time-depth functions by computing an interval velocity curve from the updated time-depth function and comparing it to the velocity log.

5 CONCLUSION

Tying wells is tedious and requires multiple processing steps. Many processes exist for tying wells but involve interpretive methods that are prone to human error. Some methods are quantitative, but ultimately, computing accurate well ties is laborious.

We incorporate DTW into a widely used process for tying wells. We use DTW to align a synthetic seismogram and a seismic trace. We apply a constant phase rotation to the synthetic and compute the optimal warping path, which corresponds to minimum $\hat{D}_i$, the sum of squared alignment errors normalized by the backtracked path length. From the optimal warping path, we compute $\tau^\star(t)$, from which we warp the synthetic to match the seismic trace, and $t^\star(\tau)$, from which we compute a new time-depth function $\tilde{\tau}_z(z)$.

Future work will involve computing an interval velocity curve from the updated time-depth function by smoothing the time-depth curve. We also look to further constrain DTW to obtain a more accurate optimal warping path. Furthermore, we will confirm that geologic formations identified from well log measurements match picked seismic horizons of the same formations when the logs are tied to the seismic trace.

DTW gives the seismic interpreter a fast estimate of a well tie. With an increase in accuracy of the synthetic seismogram and DTW constraints, DTW will give a better estimate of a well tie and updated time-depth function.

ACKNOWLEDGMENTS

Thanks to the participants in the C-team seminars who provided many suggestions that furthered this research. Thanks to Diane Witters for her collaborative review of this paper. This work was funded by the Center for Wave Phenomena and its sponsors.

REFERENCES

Anderson, T., 2009, History of geologic investigations and oil operations at teapot dome, wyoming: Presented at the 2009 AAPG Annual Convention.

Angeleri, G. P., 1983, A statistical approach to the extraction of the seismic propagating wavelet: Geophysical Prospecting, **31**, 726–747.

Connolly, P., 1999, Elastic impedance: The Leading Edge, 438–452.

Duchesne, M., and P. Gaillot, 2011, Did you smooth

your well logs the right way for seismic interpretation?: Journal of Geophysics and Engineering, **8**, 514523.

Edgar, J., and M. van der Baan, 2011, How reliable is statistical wavelet estimation?: Geophysics, **76**, V59V68.

Hale, D., 2010, Image-guided 3d interpolation of borehole data: Center for Wave Phenomena Report 656.

———, 2012, Dynamic warping of seismic images: Center for Wave Phenomena Report 723.

Mueller, M., 2007, Dynamic time warping in information retrieval for music and motion.: Springer. (318 pp.).

Sakoe, H., and S. Chiba, 1978, Dynamic programming algorithm optimization for spoken word recognition: IEEE transactions on acoustics, speech, and signal processing, **ASSP-26**.

Walden, A. T., and R. E. White, 1984, On errors of fit and accuracy in matching synthetic seismograms and seismic traces: Geophysical Prospecting, **32**, 871–891.

White, R., and T. Hu, 1997, How accurate can a well tie be?: SEG Expanded Abstracts, **16**, 816.

White, R., and R. Simm, 2003, Tutorial: Good practice in well ties: EAGE first break, **21**, 75–83.